Measuring both thermal and kinematic full-fields using a single CMOS camera during high temperature tests

T. Jailin, Nicolas Tardif, P. Chaudet, J. Desquines, M. Coret, M.-C. Baietto, V. Georgenthum

Measuring both thermal and kinematic full-fields using a single CMOS camera during high temperature tests

T. Jailin[a,b,*], N. Tardif[a], P. Chaudet[a], J. Desquines[b], M. Coret[c], M.-C. Baietto[a], V. Georgenthum[b]

[a] *Univ Lyon, INSA-Lyon, CNRS UMR5259, LaMCoS, F-69621, France*
[b] *Institut de Radioprotection et de Sûreté Nucléaire (IRSN), PSN-RES, Cadarache, Saint Paul lez Durance, France*
[c] *École Centrale de Nantes, GeM (UMR 6183), Nantes, France*

Abstract

In numerous domains, both kinematic and thermal fields are sought to study temperature dependent phenomena. They are usually obtained by digital image correlation and infrared thermography, respectively. Although these techniques are well mastered, their combination is not straightforward since they need radically different conditions to work efficiently. This paper presents a procedure to measure accurately thermal and kinematic full-fields simultaneously using a single CMOS camera in a chosen region of interest. The kinematic field is measured by global digital image correlation and the thermal field by near-infrared thermography for temperatures above 700 °C. A procedure is detailed to identify the radiometric model and compute the thermal field without being affected by the heterogeneous emissivity of the sample surface caused by the speckle pattern. A methodology showing how to manage temperature measurements during high thermal transients is also presented. The proposed approach aims to be widely accessible since it does not need strong knowledge in DIC algorithms and only requires a standard camera. The method is first validated on a virtual test case, before being used on real experiments performed at high temperature with a stereo setup.

Keywords: Full-field measurements, DIC, Thermography, High temperatures

1. Introduction

Full-field measurement techniques have been increasingly used these last years in experimental mechanics. Access to full-field data is indeed of great interest for many purposes, such as model validation, identification, or even just to help evidence activated mechanisms during experiments. In numerous domains, both kinematic and thermal fields are sought to study temperature dependent phenomena (e.g. nuclear safety, manufacturing processes, aircraft engines, etc.). Digital image correlation (DIC) is a valuable method to measure the kinematic field. It is now a mature technique, used from micro scale [1, 2] to macro scale [3] in many industrial fields. Regarding the thermal field, the most common way to measure it consists in using infrared (IR) cameras [4, 5]. Based on Planck's law, these devices convert the amount of radiation they capture in temperature data. Less common but very efficient to measure the temperature field above about 700 °C, the near-infrared (NIR) thermography technique [6, 7, 8] enables the thermal field to be measured using a standard CMOS or CCD camera.

Although IR thermography and DIC are two well mastered techniques, their combination is not straightforward since they need radically different conditions to work efficiently: DIC requires a high random gradient of gray level in the images while IR thermography needs on the contrary a well-known and homogeneous emissivity on the sample surface. Furthermore, DIC is based on the optical flow conservation assumption in the images, which may not be respected if the temperature varies during the test.

Several methods have been proposed by research teams to overcome these difficulties. Some authors for instance used two different optical systems (i.e. a standard and a IR camera) to compute the kinematic and thermal fields [9, 10]. But time and spatial interpolations remained necessary at the end to link the

*Corresponding author
Email address: author@insa-lyon.fr (N. Tardif)

two fields, which are obtained from different devices. Furthermore, no efficient solution was proposed to measure these two fields at the exact same location without having the above mentioned emissivity issue. Other authors proposed to extend the DIC technique to infrared cameras [11, 12]. However, this method needs a prior calibration step that one may want to avoid not to interfere with the material microstructure. Besides, IR cameras have often a poor spatial resolution and are relatively costly compared to standard CMOS or CCD cameras. Last but not least, this strategy needs to have both access to a DIC source code and to have some knowledge in DIC algorithms, which is not very convenient for a wide use in laboratories and industries.

An additional difficulty comes in case of fast thermal transients where the temperature is even more difficult to measure. Thermocouple measurements are not accurate during fast thermal transients due to their inertia effect [13]. The use of a pyrometer may also be complicated if a speckle pattern is present on the sample since the the emissivity will be dependent on the pattern.

This paper proposes a procedure to measure both kinematic and thermal fields using a single standard camera. The thermal field is measured by NIR thermography, and the kinematic field by DIC. A procedure is detailed to overcome the aforementioned difficulties. The key point lies in the calibration of the radiometric model used to compute the thermal field, and in a weak coupling between DIC and NIR thermography. A correction of contrast and brightness in the DIC algorithm was also used to manage the non conservation of the optical flow in the images. The method is validated on a virtual test case before being used on real experiments performed with a stereo setup [14]. In the end, this method aims to be widely usable when dealing with high temperature mechanical testing since no specific DIC or thermography software are needed. Moreover, it solely requires one standard CMOS or CCD camera.

The paper is organized as follow: first, some reminders about DIC and NIR thermography are given and the proposed method is detailed. Then, a virtual test case is presented to validate the method. Section 4 details an application of the method to real experiments performed at high temperature and with high heating rates. As an example, the method is applied here using stereo-correlation measurements. The paper finishes with some discussions and conclusions.

2. Methods

2.1. Digital image correlation (DIC)

Widely used nowadays, the digital image correlation (DIC) technique enables the kinematic full-field to be measured on a sample surface [15, 16]. This method is based on the optical flow conservation in the images during a test. When analyzing a reference image f and a deformed image g, the optical flow conservation equation reads:

$$f(\underline{x}) = g(\underline{x}+\underline{u}(\underline{x})), \tag{1}$$

where $\underline{x}$ denotes a pixel vector and $\underline{u}(\underline{x})$ the displacement field which enables g to match f. f and g are vectors containing the digital gray levels of the reference and deformed image, respectively.

The displacement field is usually found using a Gauss-Newton algorithm, minimizing the following cost function:

$$\eta^2(\underline{u}) = \sum_{\Omega} [f(\underline{x}) - g(\underline{x}+\underline{u}(\underline{x}))]^2, \tag{2}$$

where Ω is the region of interest (ROI).

This problem is ill-posed by nature and cannot be solved without regularization. In this work we used a global (or finite element) approach [17, 18], constraining the kinematic basis with finite element shape functions. The displacement field is thus described on a finite element mesh such as:

$$\underline{u}(\underline{x}) = \sum_{n} a_n.\underline{\Psi_n}(\underline{x}). \tag{3}$$

where a_n and $\underline{\Psi_n}$ are the amplitudes and the shape functions, respectively. a_n are the kinematic unknowns of the DIC problem.

It is worth reminding that 3D-surface displacement field measurements are possible if more than one camera is used. This needs a prior calibration procedure of the optical system [19, 20], which will be discussed in the following.

2.2. DIC at high temperatures

Performing DIC at high temperatures is not straightforward because the optical flow may not remain constant due to changes in radiation intensity. To overcome this problem some authors proposed to use a combination of blue bandpass filters and blue LED to avoid the influence of thermal radiations that are

at higher wavelengths [21, 22]. However, using this method precludes to perform both DIC and thermography with the same camera.

In this work the open source DIC software UFreckles [23] was used. In order to manage the non-conservation of the optical flow a correction of contrast and brightness is performed in all the elements at each time step of the DIC process. This correction is achieved using the Zero-Normalized Sum of Squared Differences (ZNSSD) matching criterion implemented in UFreckles. In all images, the gray levels in each element are affinely transformed so that they have a zero mean value and a unit standard deviation. The minimization problem being over-constrained by the finite element regularization, the DIC algorithm still succeeds to capture all the kinematic on the sample despite the additional degrees of freedom. This will be demonstrated on a virtual test case in the following section.

Calibration of the optical system is required to derive 3D-surface full-field from stereo correlation. To avoid chromatic aberrations during the tests, the focus and the calibration must be performed at the same wavelength as at high temperatures. To do so, the sample, which is used to calibrate the stereovision model, was lighted during the calibration process at room temperature with a near-infrared LED at a wavelength of 860 nm. Near-infrared bandpass filters at the same wavelength were mounted on the cameras to take the calibration images. The 860 nm wavelength was chosen to be the most excited one on Zircaloy-4 around 850 °C, which are the conditions of our study. Doing so, the optical system was calibrated at room temperature prior to the test in optical conditions representative of high temperatures.

2.3. Near-infrared thermography (NIRT)

The near-infrared thermography (NIRT) technique [6, 7] is used to compute the temperature full-field on the surface of an object using a standard CMOS camera. This technique is based on the fact that each object emits a certain amount of spectral radiation depending on its temperature. Using Planck's law and Wien's approximation it is possible to obtain a direct relation between the digital level of an image I (i.e. the gray level of the pixels) and the temperature T such as:

$$T(\underline{x}) = \frac{K_1}{\ln\left(\frac{K_2}{I(\underline{x})} + 1\right)}, \tag{4}$$

where $\underline{x}$ denotes a pixel vector and K_1 et K_2 are two constants defined by:

$$K_1 = \frac{h.c}{k_B.\lambda_e} \tag{5}$$

and

$$K_2 = 2.\varepsilon(\lambda_e).c^2.\lambda_e^{-4}.W(\lambda_e).t_i.K_{int}, \tag{6}$$

where h is the Planck's constant, c is the light speed, k_B is the Boltzmann's constant, λ_e is the effective wavelength, ε is the emissivity, W is the spectral response of the acquisition chain, t_i is the integration time and K_{int} is an integration constant. More details on the construction of Equation (4) can be found in [6].

Assuming homogeneous and stable emissivity, and using the notion of effective wavelength K_1 and K_2 can be set as constants. Using a calibration point on the images (i.e. a point where the temperature is known on the images) it becomes possible to identify the two constants and compute the thermal profile on the surface of the object of interest. Some points need nonetheless to be discussed:

(i) the temperature needs to be high enough to enable standard cameras to be sensitive to the spectral radiations. This minimal temperature value depends on the material and is about 700 °C for metals.

(ii) the radiometric model depends on the emissivity of the object. To avoid errors, the emissivity must remain constant during the whole test and be homogeneous in the region of interest (ROI) where the temperature full-field is computed. This may be an issue considering a speckle pattern deposited over the sample to perform DIC. A method is proposed in the following to tackle this problem.

(iii) the radiometric model described in Equation (4) is based on the notion of effective wavelength λ_e, which may not be very accurate if a large range of temperature is measured. In this case it is possible to improve the result by linking the effective wavelength to the temperature, leading to the extended effective wavelength, as proposed in [6, 24]. It is also possible to use a bandpass filter to limit the wavelength spectrum measured by the camera. This latter option was chosen in the present work.

(iv) finally, the shape of the object may have an impact on its apparent emissivity [25]. This must be considered when dealing with non-planar objects. This will be

discussed at the end of this work.

2.4. Manage the heterogeneous emissivity on the sample to compute the thermal field

As already mentioned, the speckle pattern leads to a heterogeneous emissivity onto the sample surface. In order to use a single emissivity value in the radiometric model only one tint of paint must be used in the images to compute the thermal field. The tests are performed within an enclosure where the atmosphere is controlled with an argon flush to avoid oxidation of the sample. However, little oxidation can still occur at high temperature. An oxide layer can grow during the tests between the sample outer surface and the paint. Since the oxide layer is black, the emissivity of the white paint may be significantly impacted by the oxide growth. It is therefore preferable to perform the NIR thermography on the black paint not to be affected by emissivity changes. A new parameter P is then defined to identify the pixels corresponding to the black paint. It is used as a threshold to select the brightest pixels in the images since the black paint has an highest emissivity. Only these pixels were used to identify the radiometric model and compute the thermal field.

One may notice that if the temperature is not uniform on the sample using only the $P\%$ brightest pixel may not be sufficient to ensure that only the black paint is used through the radiometric model. Gray or white painted areas at a higher temperature may have a higher intensity in the images than black paint at lower temperatures. Errors would then appear because multiple emissivities would be used with the same radiometric model. To overcome this, a weak coupling between the DIC and the NIRT was developed. Two assumptions were first formulated:

(i) the temperature is averaged within each element of the correlation mesh;

(ii) the $P\%$ of the brightest pixels within an element correspond to the black paint (only these pixels are then used to compute the thermal field).

These two assumptions enable computing accurately the thermal field at each time step on the deformed correlation mesh without being affected by the heterogeneous emissivity of the sample surface. Yet, the value of the parameter P needs to be defined. If all the pixels in the elements are used, or if the parameter P is too high, the average emissivity of each element would depend on the fraction of black and white paints in each element. This would induce errors in the temperature field since the radiometric model must be used with a single emissivity. On the contrary if not enough pixels are used, the influence of noise in the images becomes more important. In our case, a value ranging from 5% to 20% can be used without visible differences to obtain good results. This range depends on the number of pixels within the elements and of the speckle pattern distribution. A value of 10% was used in this study.

This method leads to a very smooth thermal field, because non-affected by the speckle pattern. It is also a good point to notice that no interpolation was necessary between the kinematic and thermal fields, both being computed on the same mesh.

3. Application to a 2D virtual test case

3.1. Description of the test case

In order to validate the method, a virtual test case, reproducing a tensile experiment at high temperature, was setup. The flow chart presented in Figure1 details the different steps of the virtual test case.

The reference image of the virtual sample (cf. Figure 2) was obtained from one of the real experiments presented in the next section.

Fifty deformed images were generated by adding a virtual strain field and a virtual temperature field on the reference image. The tensile strain field was applied with strain values ranging from 0 to 18 %. The y-displacement field applied is given in Equation (7). The x-displacement field was applied using a Poisson's ratio of 0.35. The y-displacement field at the last step can be observed in Figure 2.

$$U_y(t,y) = y.\exp\left(\frac{t}{10}\right), \tag{7}$$

where t and y denote the time step and the y-coordinate of the pixel, respectively.

The virtual temperature evolution was applied onto the deformed images using the radiometric model described in Equation (4) and the constant values given in Table 1. The temperature evolution applied on the sample is described in Figure 3. An oscillation of 70 °C was imposed with a hot-spot located at the center of the sample. The temporal evolution $\delta(t)$ was described using a sinus function and the hot spot shape $\varphi(x,y)$ using the equation of a circle, as follow:

$$\delta(t) = 35.\sin\left(\frac{t}{5}\right), \tag{8}$$

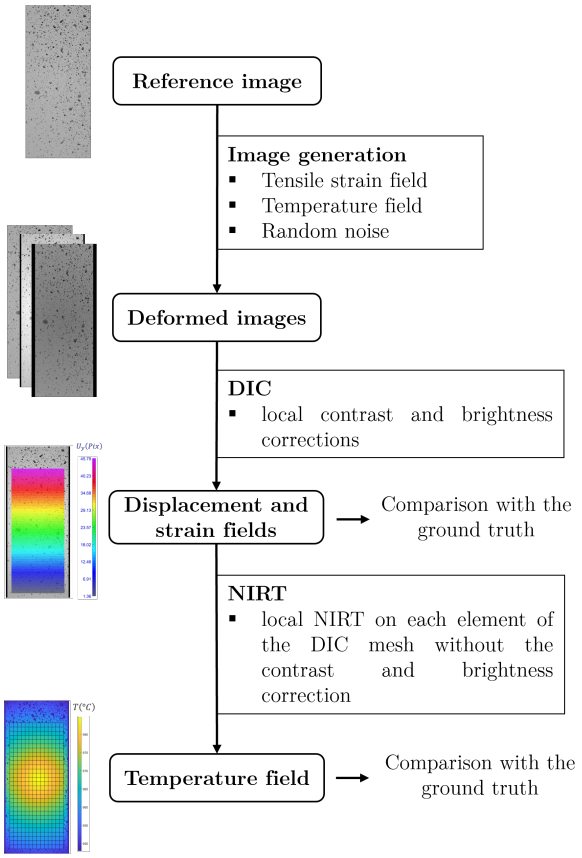

Figure 1: Flow chart presenting the different steps of the virtual test case.

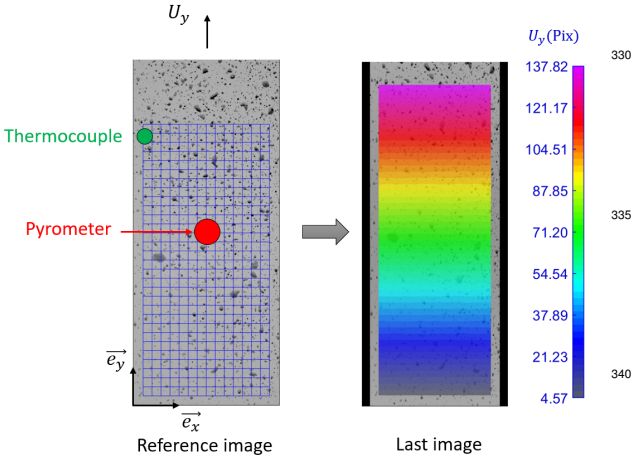

Figure 2: Example of an image obtained from a real experiment performed at 950 °C. The virtual pyrometer and thermocouple locations are shown in red and green, respectively. The deformed image generated for the last step of the virtual test case is also presented with the y-displacement field.

$$\varphi(x,y) = 1 - \sqrt{\frac{(x-x_0)^2 + (y-y_0)^2}{\left(\frac{y_M}{2}\right)^2 + \left(\frac{x_M}{2}\right)^2}}, \qquad (9)$$

where t is the time step, (x,y) is the pixel position, (x_0,y_0) is the center of the image, (x_M,y_M) is the image resolution.

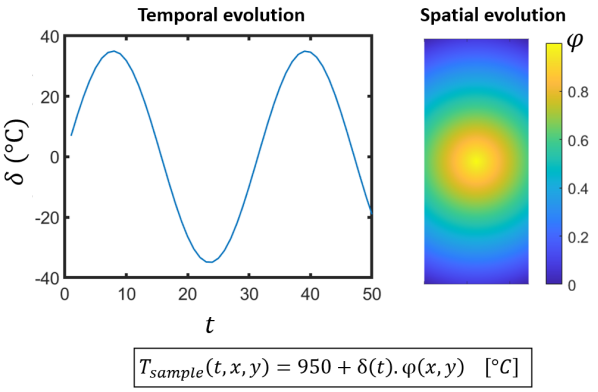

Figure 3: Temperature impose to the sample during the virtual test. $T_{sample}(t,x,y)$ is the temperature of the sample at the time t and pixel position (x,y). δ and φ are described in Equations (8) and (9), respectively.

After the generation of the virtual deformed images, a random noise (white noise with a standard deviation of 1.8 gray level) was added in all the images to reproduce real experimental conditions. The values of the two constants used in the radiometric model were finally forgotten and will have to be re-identified.

The temperature is supposed to be known at a virtual thermocouple located at the boundary of the sample (cf. Figure 2). In some cases, pyrometric measurements are necessary no to be affected by the inertia effect of the thermocouples [13]. This requires to know the emissivity of the spot area pointed by the pyrometer. If DIC is performed the emissivity may not be identical on each sample because of the speckle pattern (or of the natural texture of the surface). Depending on the material, it may be impossible to identify the sample emissivity prior to the test without interfering with the metallurgical state of the material.

A procedure has been developed in this work to be able to use a pyrometer without knowing the emissivity of the sample surface before the tests. The emissivity of the pyrometer must be first set to an arbitrary value, close to the expected value. It will have to be corrected

after the test to obtain correct pyrometer measurements. Additionally to the two constants of the radiometric model, a third unknown ε_{pyro} has then to be identify, being the true emissivity at the pyrometer pointing location. In order to validate the method in the most demanding case, a pyrometer pointing at the center of the sample is simulated in this virtual test case (cf. Figure 2). The true emissivity of the sample is set to 0.89. The pyrometer data are then generated with a wrong emissivity of 0.83 in order to be representative of the real experiments where the true emissivity is not known prior to the tests because of the speckle pattern.

Once all the data of the virtual test case is generated, the global DIC analysis is performed on the images using quadrilateral elements with linear shape functions. The element size was set to 35x35 Pix^2 (1 Pix $\simeq$ 9 μm) to be representative of the real experiments presented in the nex section. The correlation mesh used can be seen in Figure 2.

3.2. Identification procedure

The pyrometer emissivity cannot directly be identified using the thermocouple data since the pyrometer and the thermocouple are not located at the same position. The NIR thermography is then used as a bond to link the different devices. The three parameters $\{K_1, K_2, \varepsilon_{pyro}\}$ are identified by minimizing the following cost-function:

$$er^2 = \left(T_{TC}^{NIRT} - T_{TC}\right)^2 + \left(T_{pyro}^{NIRT} - T_{pyro}\right)^2, \qquad (10)$$

where T_{TC} is the temperature measured by the thermocouple, T_{pyro} is the temperature measured by the pyrometer, T_{TC}^{NIRT} is the temperature obtained by NIR thermography at the thermocouple welding vicinity, and T_{pyro}^{NIRT} is the temperature obtained by NIR thermography at the pyrometer pointed area. As a reminder, only the 10% brightest pixels were used to compute the temperature by NIR thermography at the pyrometer and thermocouple areas.

This cost function gathers the temperature data of all the time steps in order to use the largest range of temperature and identify the three parameters as accurately as possible.

3.3. Results of the test case

Figure 4 presents a comparison of the y-displacement at the top of the correlation mesh between the values obtained by DIC and the ground truth (i.e. the well-known imposed displacement). The mean error is about 0.15 pixel, which is considered to be very good.

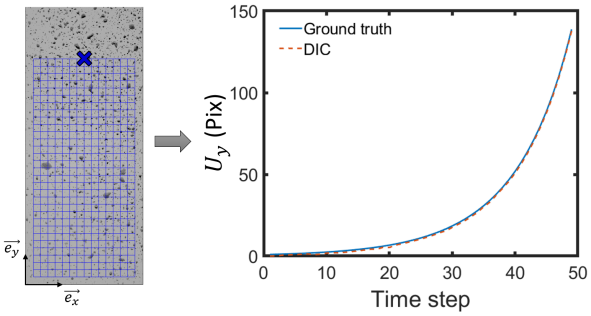

Figure 4: Comparison of the vertical displacement U_y at the blue cross between the ground truth and the displacement obtain by DIC.

Different residual maps are presented in Figure 5 for the last image of the test. The left map shows the residual field obtained at the very beginning of the DIC process (i.e. without both the local contrast and brightness correction and the displacement field correction). The error is then a sum of the error due to the temperature variation and to the displacement. The middle-left map presents the residual field obtained at the initial iteration of the DIC algorithm but with the local contrast and brightness correction. It can be observed that the error is now mainly due to the displacement in the images and that the effect of temperature has been successfully removed. The middle-right map shows the residual field obtained at the converged iterations of the DIC algorithm. As a matter of comparison, the residual field solely caused by the noise in the images is also presented. To obtain the latter, an image was generated without deformation and at the same temperature than the reference image. The differences between the two images are then only due to the noise added virtually onto the images at the end of the image generation process. A DIC analysis was then performed between these two images. The displacement field obtained was as expected (almost) the null field, and the residual field obtained was (almost) similar to the noise field applied onto the images. Because of the nature of the noise, the best residual field (i.e. with the smallest absolute values) that can be obtained with DIC is the noise residual map. It is then a very useful tool for comparison purposes. It can be observed in Figure 5 that the converged residual map is very low, almost equal to the residual map solely caused by noise. It shows that the DIC algorithm captured the kinematic on the sample very well, despite the non-conservation of the optical flow.

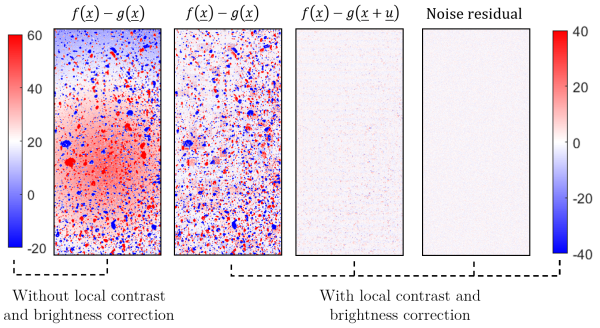

Figure 5: Residual maps obtained at the end of the virtual test case: (left map) at the beginning of the DIC process; (middle-left) at the initial iteration of the DIC algorithm with local and brightness correction; (middle-right) at the last iteration with local and brightness correction; (right) approximated residual map solely caused by noise. The error is expressed in gray level.

The two constants of the radiometric model as well as the corrected emissivity are then identified. The temperature field obtained at the 8^{th} time step is given in Figure 6 with the true applied field. This time step is the most demanding one since it is when the thermal gradient is the most important. The average error obtained is about 0.4 °C. It can be observed that the error is mostly positive. This is due to the noise added to the images and to the assumptions stated in section 2.4. Since only the brightest pixels are used to compute the thermal field, the temperature obtained by NIR thermography is slightly higher than the average one in the elements. When the thermal gradient is low (e.g. time step 16), the maximal error is about 0.1 °C.

The comparison between the real parameters and the identified ones is given in Table 1. Very low differences are found for the emissivity and K_1. K_2 is a bit higher than the initial value because it adapts both the noise impact and the assumption stating that the temperature within an element is homogeneous. The comparison in the temperature data shows that the method is very effective to compute the thermal field onto speckle patterned samples at very high temperature.

	Emissivity	K_1	K_2
Ground truth	0.89	1.560×10^4	5.91×10^7
Identified	0.8897	1.553×10^4	4.78×10^7
Error (%)	0.03	1.8	19.0

Table 1: Comparison of the parameter values between the ground truth and the identified values.

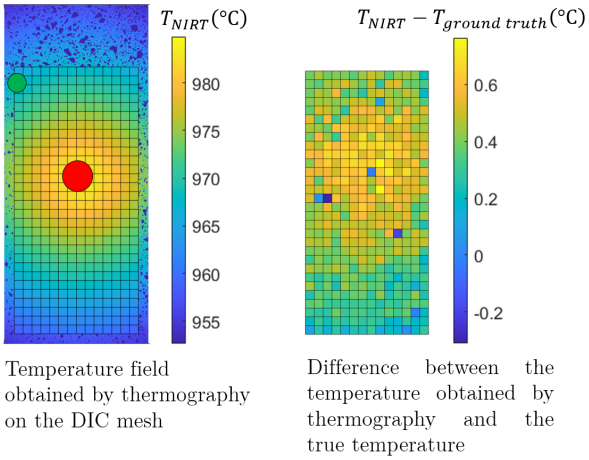

Temperature field obtained by thermography on the DIC mesh

Difference between the temperature obtained by thermography and the true temperature

(a)

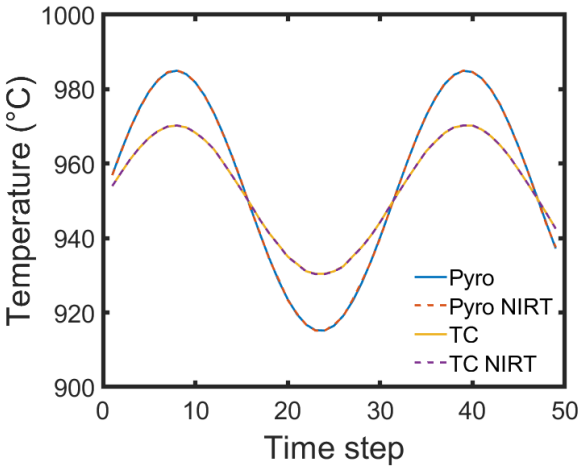

(b)

Figure 6: Results of the NIR thermography for the virtual test case. (a) The left plot shows the temperature field computed on the DIC mesh at the 8^{th} time step. The pyrometer and the thermocouple location are shown in red and green, respectively. A comparison of the temperature field between the one measured by NIR thermography and the ground truth is also presented. (b) Difference in the temperature field between the thermal field obtained by NIR thermography and the ground truth.

4. Application to real experiments

4.1. Experimental setup

The method is now applied on real experiments which were presented in [14]. The experimental setup ELLIE used in this work is first briefly described, more details can be found in the previous reference. It is worth noting that a stereo optical system was used in these experiments to reconstruct the 3D-surface fields. The present method can be used either for 2D DIC or stereo measurements, since the only difference between these two techniques is a 3D reconstruction step, which does not affect the method presented in this work.

The test bench ELLIE is composed of a 10 kN servo-hydraulic tensile machine (cf. Figure 7). The tubular sample is connected onto the test machine using custom grips [26]. An internal pressure up to 70 bar can be imposed and controlled within the specimen during the whole tests using argon gas. A 30kW induction generator (ThermoInduzione TI3-30KW CT-110) is used to heat the samples with heating rates up to 1500 °C/s. The induction generator frequency (92 kHz) was chosen so that the thermal loading is uniform across the wall-thickness of the sample. The temperature regulation is achieved using a pyrometer (CTLM-2HCF4-C3, wavelength of 1.6 μm). All the experiments were performed within an enclosure where an argon flush was set up during the tests to prevent sample oxidation.

The specimens were cut from fuel claddings made of Zircaloy-4 alloy. They were 90 mm long with an outer diameter of 9.5 mm and a wall-thickness of 0.57 mm. In order to perform stereo-correlation measurements the specimens were painted with a black undercoating and a white speckle pattern. Three thermocouples (type K, wires of 79 μm diameter) were spot-welded on the sample outer surface in the region of interest (ROI) seen by the cameras (cf. Figure 7).

The test procedure aimed at reproducing simulated thermo-mechanical conditions of a reactivity initiated accident (cf. Figure 8). The cladding was first internally pressurized with pressure levels ranging from 7 to 11 bar. Once the pressure was stabilized the sample was heated up in open loop with heating rate of about 1200 °C/s. The thermal regulation switched in closed loop control (i.e. with feedback) when the temperature measured by the pyrometer reached a value 20 °C lower than the target temperature. Temperatures of interest ranged from 840 to 1020 °C. A compressive force was also applied on the sample simultaneously to the internal pressure to compensate the end caps effect. This force was calculated using the initial inner radius R_i of the claddings and the internal pressure P_i applied:

$$F_z = P_i.\pi.R_i^2. \tag{11}$$

Two CMOS cameras, separated by an angle of 18 °, were used to record images of the sample during the tests at a frequency of 55 Hz. An example of an image is given in Figure 9. It is worth pointing out that since the black paint has a higher emissivity than the white paint, the black paint appears in white in the images at high temperature and the white paint appears in black. The image acquisition parameters and the DIC parameters are given in Tables 2 and 3, respectively.

4.2. Identification procedure

As in the virtual test case, the parameters $\{K_1, K_2, \varepsilon_{pyro}\}$ need to be identified. The identification procedure is however slightly different than in the previous case because the thermocouples are not reliable during the thermal transient due to their inertia effect [13]. An identification procedure of the three parameters is proposed below. Two error functions are first defined:

$$er_1^2 = \left(T_{TC}^{NIRT} - T_{TC}\right)^2, \tag{12}$$

$$er_2^2 = \left(T_{pyro}^{NIRT} - T_{pyro}\right)^2, \tag{13}$$

where T_{TC} is the temperature measured by the thermocouples, T_{pyro} is the temperature measured by the pyrometer, T_{TC}^{NIRT} is the temperature obtained by NIR thermography at the thermocouple areas, and T_{pyro}^{NIRT} is the temperature obtained by NIR thermography at the pyrometer area.

er_1^2 uses only the data during the thermal plateau once the thermocouples are stabilized. er_2^2 uses all the temperature data in the plateau and during the thermal transient in order to cover a wide range of temperature. The three parameters are then identified by minimizing the sum of these two cost functions using a Gauss-Newton algorithm. This process enables the parameters to be identified without being affected by the inertia effect of the thermocouples and using a large range of temperature.

4.3. Results

Figure 10 shows an example of a thermal and a kinematic field obtained during a test performed at 880 °C and 11 bar. A 3D-surface reconstruction of the

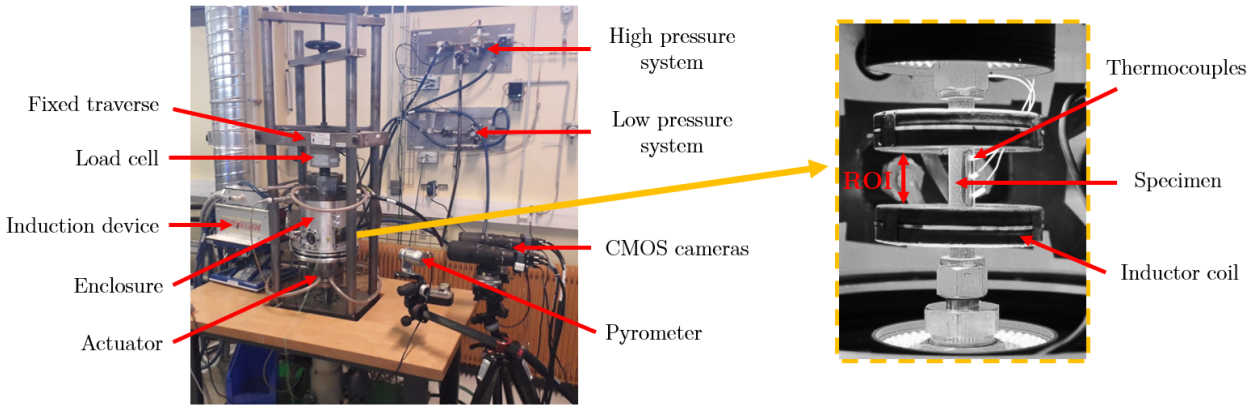

Figure 7: ELLIE setup with a view of the sample within the enclosure - left: general overview of the setup, right: inside the enclosure view.

Cameras	CMOS, VC-12MC-M65E0-FM
Lens	NIK AF MICRO-NIKKOR 200MM F/4 D IF-ED
Bandpass filter	Wavelength λ = 865nm +/-10nm
Angle between the cameras	18 °
Image resolution	12 MPix (4096 $\times$ 3072)
Dynamic range	8 bits
Acquisition rate	55 Hz
Image scale	1 Pix $\simeq$ 9 μm
Patterning technique	Black undercoating, white spray painting

Table 2: Image acquisition parameters.

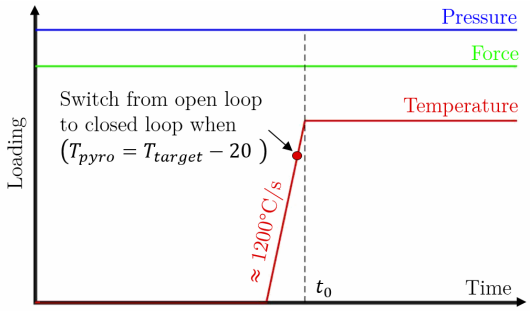

Figure 8: Test procedure.

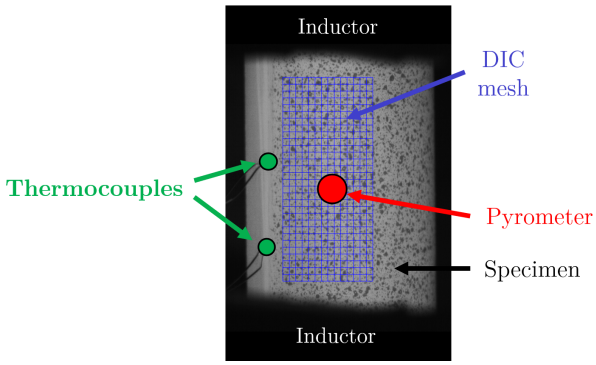

Figure 9: Example of an image recorded by the right camera. The pyrometer is pointing at the center of the ROI (red point). The correlation mesh used to perform the global DIC is shown in blue.

DIC Software	UFreckles v2.1 [23]
Element size	35× 35 Pix^2
Element type	Linear quadrilateral element
Filtering operation	None
Matching criterion	Zero-mean Normalized Sum of Squared Differences (ZNSSD)

Table 3: DIC parameters.

ROI is also given. Since a stereo setup was used, the kinematic and the thermal fields can both be obtained in 3 dimensions on the ROI. It can be observed that the two fields are smooth while no smoothing operations were used. Since many pixels are used in each element to compute the NIR temperature and that the noise over signal ratio is low in the images, it follows that the uncertainty of the thermal field can be approached by the uncertainty of the calibration point. According to the manufacturer documentation and in our application case, the thermocouple and pyrometer uncertainties are about 0.6% of the true temperature.

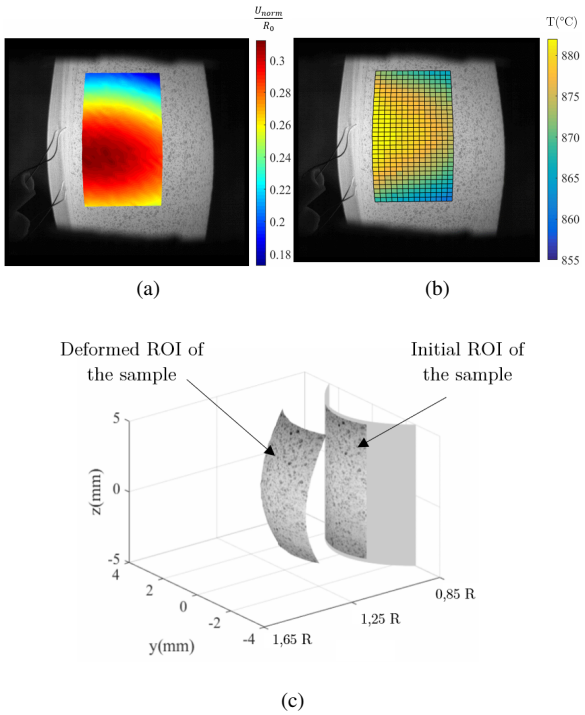

Figure 10: Example of results obtained during a test performed at 880 °C and 11 bar: (a) displacement field computed by stereo-correlation and normed by the initial radius of the sample R_0 ; (b) thermal field obtained by NIR thermography; (c) 3D reconstruction of the ROI.

Figure 11 shows the residual map obtained at the initial and converged stage of the DIC algorithm. As a matter of comparison, the approximated residual map solely due to noise is also presented. To obtain the latter, a sample was heated to 1000 °C without internal pressure. Once the temperature was stabilized 50 images were recorded at 55 Hz. Since there was no mechanical loading and that the material was at equilibrium the differences between the images were only due

to noise. A DIC analysis was then performed between these images to estimate the noise residual map. For each residual field, the standard deviation σ of the error is also given. It can be observed that the kinematic has been well captured by the DIC. Tiny stains of errors can be seen and are due to paint damaging after eyes checking. A noise sensitivity evidenced noise levels of about 1 μm on the in-plane displacement and of about 5 μm on the out-of-plane displacement. These values of noise result from the combined influence of several factors like the camera resolution, DIC algorithms, etc. In Figure 11 it can be observed that converged residual map is finally closed to the noise map, having a factor 2 between their standard deviation values.

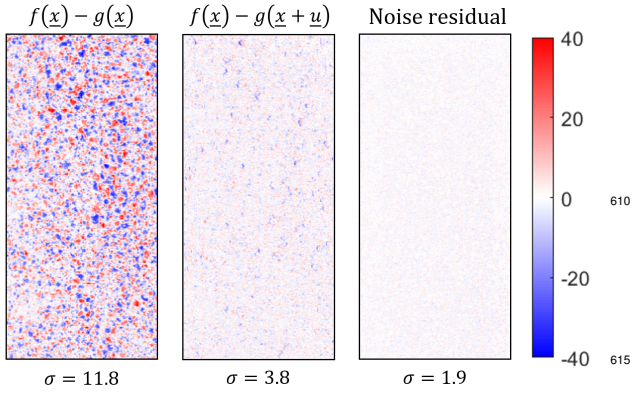

Figure 11: Residual maps obtained during the tests at the first and last iteration of the DIC algorithm (two left maps). The right map shows the approximated residual map solely caused by noise. The error is expressed in gray level.

Figures 12 shows the thermal results obtained for an experiment carried out at 970 °C. Only the results of the first seconds of the test were sought here. The heating rate was too high to obtain a perfect temperature ramp and a sharp transition at the temperature plateau, but this is even more interesting to have this richer data for identification proposes [27]. It can be observed that the pyrometer data matches well the NIR thermography all test long. During the first seconds of the test a small difference can be noticed between the thermocouples and the thermography, which is due to the inertia effect of the thermocouples during the heating. This error finally decreases when the temperature stabilizes.

4.4. Discussion

Impact of the sample shape

The apparent emissivity of an object is dependent of the observation angle [25] (i.e. the angle between the camera and the normal to the sample surface). Given the tubular geometry of the sample, the impact of the shape on the emissivity has been studied. A specimen was heated from room temperature to 1200 °C in a GLEEBLE-3500 device. Thanks to the grips and to the thermal conduction across the sample, the temperature field obtains on the tubular specimen is axisymmetric [13]. Using a standard camera, the well known geometry of the specimen, and the Equation (4) it is possible to compute the variation of emissivity on the sample as a function of the observation angle. As an example, the emissivity is shown as a function of the observation angle in Figure 13 for a specimen heated to 1000 °C. It can be seen that no significant impact is observed up to an observation angle of 60°. Above this value the emissivity significantly decreases. If needed, corrections at the first order can be taken into account into the radiometric model to limit the errors. The authors remind that these results are dependent on the wavelength of the thermal radiations, and of the roughness and surface of the specimens (i.e. painted, raw, oxidized...). Depending on these parameters it may be worth to study this effect when performing IR thermography with a stereo setup since at least one camera will have a non-null observation angle.

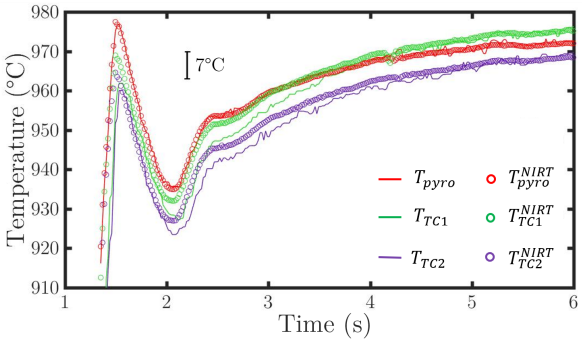

Figure 12: Comparison of the temperature measured by the pyrometer and thermocouples to the temperatures computed by NIR thermography at the same locations. The uncertainty bar comes from the thermocouple documentation at this level of temperature.

Impact of the heat haze effect

One may also be careful to the haze effect, which can be observed when performing tests at high temperature [28]. In our case, the vertical position of the sample and the argon flush during the tests enabled not to be impacted by the haze effect. Using a gas flush, a fan or positioning the sample vertically can contribute to reduce the haze effect.

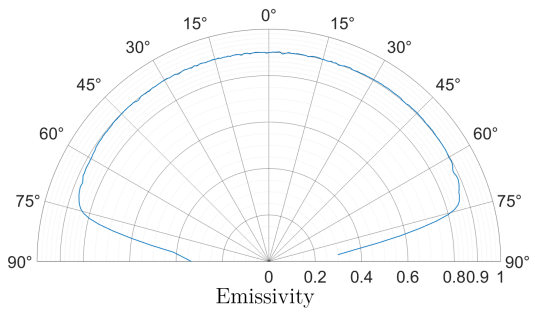

Figure 13: Evolution of the emissivity with the observation angle. The emissivity at 0° is here arbitrary set equal to 0.9. These results were obtained using the black paint on a sample heated to 1000 °C.

5. Summary and conclusions

A procedure to measure simultaneously kinematic and thermal fields with a single standard camera has been presented. It uses the global DIC method to measure the kinematic field and the NIR thermography method to compute the thermal field. Based on a simple weak coupling, between DIC and thermography, a method is proposed to manage the presence of a speckle pattern when using thermography. The thermal field obtained is finally smooth and no interpolation is needed to match the data with the kinematic field. An identification strategy for the radiometric model has also been proposed to perform accurate temperature measurements during fast thermal transients.

The method was first validated on a virtual test case, and was then applied in 3D using real experiments performed at high temperatures. Same levels of errors were obtained in the virtual test case and in the real experiments showing that the method can be applied accurately with a stereo setup. The proposed method showed a very good robustness even at temperatures greater than 1000 °C and with strain levels above 30%. Smooth 3D-surface thermal and kinematics full-fields were finally obtained, leading to very rich experiments where various temperature and loading conditions were obtained at the same time.

The proposed method aims to be widely useful for any mechanical testing at above 700 °C. It does not require any specific software or device and showed a very good robustness in severe conditions. If one wants to measure thermal fields with strong temporal evolution of the temperature he may nevertheless be impacted by over-saturated (or under-saturated) images. Using multi-exposure time or a PID regulation of the exposure time of the cameras, as proposed in [8], could be considered to overcome this issue.

Acknowledgments

The authors acknowledge with thanks financial support of this work from EdF and Institut Carnot Ingénierie@Lyon. The authors want also to express their thanks to J. Réthoré for allowing access to the UFreckles software and ATYS Consulting Group for helping on the induction problematic.

References

[1] E. Salvati, A. M. Korsunsky, An analysis of macro- and micro-scale residual stresses of Type I, II and III using FIB-DIC micro-ring-core milling and crystal plasticity FE modelling, International Journal of Plasticity 98 (2017) 123–138. doi:10.1016/j.ijplas.2017.07.004.

[2] A. Orozco-Caballero, T. Jackson, J. Q. da Fonseca, High-resolution digital image correlation study of the strain localization during loading of a shot-peened RR1000 nickel-based superalloy, Acta Materialia 220 (2021) 117306. doi:10.1016/j.actamat.2021.117306.

[3] C. Jaafari, D. Bertrand, T. Guillot, E. Prudhomme, N. Tardif, J.-F. Georgin, F. Delhomme, R. Trunfio, N. Chateur, E. Bruyere, E. Augeard, L. Baillet, P. Guéguen, S. Grange, Effect of early age drying shrinkage on the seismic response of RC structures, Materials and Structures 53 (6) (2020) 133. doi:10.1617/s11527-020-01552-2.

[4] J. Artozoul, C. Lescalier, O. Bomont, D. Dudzinski, Extended infrared thermography applied to orthogonal cutting: Mechanical and thermal aspects, Applied Thermal Engineering 64 (1) (2014) 441–452. doi:https://doi.org/10.1016/j.applthermaleng.2013.12.057.

[5] W. Harizi, S. Chaki, G. Bourse, M. Ourak, Mechanical damage assessment of glass fiber-reinforced polymer composites using passive infrared thermography, Composites Part B: Engineering 59 (2014) 74–79. doi:https://doi.org/10.1016/j.compositesb.2013.11.021.

[6] Y. Rotrou, T. Sentenac, Y. Le Maoult, P. Magnan, J. Farré, Near infrared thermography with silicon FPA - Comparison to MWIR and LWIR thermography, Quantitative InfraRed Thermography Journal 3 (1) (2006) 93–115. doi:10.3166/qirt.3.93-115.

[7] D. Campello, N. Tardif, J. Desquines, M. C. Baietto, M. Coret, A. Maynadier, P. Chaudet, Validation of a multimodal set-up for the study of zirconium alloys claddings' behaviour under simulated LOCA conditions, Strain 54 (5) (2018) 1–14. doi:10.1111/str.12279.

[8] C. Zhang, J. Marty, A. Maynadier, P. Chaudet, J. Réthoré, M. C. Baietto, An innovative technique for real-time adjusting exposure time of silicon-based camera to get stable gray level images with temperature evolution, Mechanical Systems and Signal Processing 122 (2019) 419–432. doi:10.1016/j.ymssp.2018.12.042.

[9] L. Bodelot, L. Sabatier, E. Charkaluk, P. Dufrénoy, Experimental setup for fully coupled kinematic and thermal measurements at the microstructure scale of an AISI 316L steel, Materials Science and Engineering: A 501 (1-2) (2009) 52–60. doi:10.1016/j.msea.2008.09.053.

[10] A. Chrysochoos, B. Berthel, F. Latourte, A. Galtier, S. Pagano, B. Wattrisse, Local energy analysis of high-cycle fatigue using digital image correlation and infrared thermography, The Journal of Strain Analysis for Engineering Design 43 (6) (2008) 411–421. doi:10.1243/03093247JSA374.

[11] A. Maynadier, M. Poncelet, K. Lavernhe-Taillard, S. Roux, One-shot Measurement of Thermal and Kinematic Fields : InfraRed Image Correlation (IRIC), Experimental Mechanics 52 (3) (2012) 241–255. doi:10.1007/s11340-011-9483-2.

[12] A. Charbal, S. Roux, F. Hild, L. Vincent, Spatiotemporal regularization for digital image correlation: Application to infrared camera frames, International Journal for Numerical Methods in Engineering 114 (12) (2018) 1331–1349.

[13] T. Jailin, N. Tardif, J. Desquines, M. Coret, M. Baietto, V. Georgenthum, Experimental study and modelling of the phase transformation of Zircaloy-4 alloy under high thermal transients, Materials Characterization 162. doi:10.1016/j.matchar.2020.110199.

[14] T. Jailin, N. Tardif, J. Desquines, P. Chaudet, M. Coret, M.-C. Baietto, V. Georgenthum, Thermo-mechanical behavior of Zircaloy-4 claddings under simulated post-DNB conditions, Journal of Nuclear Materials 531. doi:10.1016/j.jnucmat.2020.151984.

[15] M. Sutton, W. Wolters, W. Peters, W. Ranson, S. McNeill, Determination of displacements using an improved digital correlation method, Image and Vision Computing 1 (3) (1983) 133–139. doi:10.1016/0262-8856(83)90064-1.

[16] B. D. Lucas, T. Kanade, An iterative image registration technique with an application to stereo vision, in: IJCAI, Vancouver, 1981, pp. 674–679.

[17] G. Besnard, F. Hild, S. Roux, "Finite-element" displacement fields analysis from digital images: application to Portevin-Le Châtelier bands, Experimental Mechanics 46 (6) (2006) 789–803. doi:10.1007/s11340-006-9824-8.

[18] J. Réthoré, T. Elguedj, P. Simon, M. Coret, On the Use of NURBS Functions for Displacement Derivatives Measurement by Digital Image Correlation, Experimental Mechanics 50 (7) (2010) 1099–1116. doi:10.1007/s11340-009-9304-z.

[19] M. A. Sutton, J. J. Orteu, H. Schreier, Image Correlation for Shape, Motion and Deformation Measurements, Springer Science & Business Media, 2009.

[20] M. Grédiac, F. Hild, Full-field measurements and identification in solid mechanics, Wiley Online Library, 2013.

[21] B. M. Grant, H. J. Stone, P. J. Withers, M. Preuss, High-temperature strain field measurement using digital image correlation, Journal of Strain Analysis for Engineering Design 44 (4) (2009) 263–271. doi:10.1243/03093247JSA478.

[22] T. Archer, P. Beauchene, C. Huchette, F. Hild, Global digital image correlation up to very high temperatures with grey level corrections, Measurement Science and Technology 31 (2) (2019) 024003.

[23] J. Réthoré, UFreckles v2.1 (2018). doi:10.5281/zenodo.1433776.

[24] P. Saunders, General interpolation equations for the calibration of radiation thermometers, Metrologia 34 (3) (1997) 201–210. doi:10.1088/0026-1394/34/3/1.

[25] X. He, Y. Li, L. Wang, Y. Sun, S. Zhang, High emissivity coatings for high temperature application : Progress and prospect, Thin Solid Films 517 (17) (2009) 5120–5129. doi:10.1016/j.tsf.2009.03.175.

[26] N. Tardif, M. Coret, A. Combescure, Experimental study of the fracture kinetics of a tubular 16MnNiMo5 steel specimen under biaxial loading at 900 and 1000°C . Application to the rupture of a vessel bottom head during a core meltdown accident in a pressurized water reactor, Nuclear Engineering and Design 241 (3) (2011) 755–766. doi:10.1016/j.nucengdes.2011.01.026.

[27] T. Jailin, N. Tardif, J. Desquines, P. Chaudet, M. Coret, M.-C. Baietto, V. Georgenthum, FEMU based identification of the creep behavior of Zircaloy-4 claddings under simulated RIA thermo-mechanical conditions, Journal of Nuclear Materialsdoi:10.1016/j.jnucmat.2022.153542.

[28] M. Berny, T. Archer, A. Mavel, P. Beauchêne, S. Roux, F. Hild, On the analysis of heat haze effects with spacetime dic, Optics and Lasers in Engineering 111 (2018) 135–153. doi:https://doi.org/10.1016/j.optlaseng.2018.06.004.